Measurements of neutron-induced fission cross sections for ^{209}Bi, ^{nat}Pb, ^{208}Pb, ^{197}Au, ^{nat}W, and ^{181}Ta in the intermediate energy region

A. N. Smirnov,* V. P. Eismont, and N. P. Filatov
V. G. Khlopin Radium Institute, 2oi Murinskiy Prospect 28, Saint-Petersburg 194021, Russia

J. Blomgren† and H. Condé
Department of Neutron Research, Ångström Laboratory, Uppsala University, Box 525, S-751 20 Uppsala, Sweden

A. V. Prokofiev‡
The Svedberg Laboratory, Uppsala University, Box 533, S-751 21 Uppsala, Sweden
and V. G. Khlopin Radium Institute, 2oi Murinskiy Prospect 28, Saint-Petersburg 194021, Russia

P.-U. Renberg
The Svedberg Laboratory, Uppsala University, Box 533, S-751 21 Uppsala, Sweden

N. Olsson
Department of Neutron Research, Ångström Laboratory, Uppsala University, Box 525, S-751 20 Uppsala, Sweden
and Swedish Defense Research Agency (FOI), S-172 90 Stockholm, Sweden
(Received 8 July 2004; published 4 November 2004)

Neutron-induced fission cross-section ratios ^{nat}Pb/^{209}Bi, ^{208}Pb/^{209}Bi, ^{197}Au/^{209}Bi, ^{nat}W/^{209}Bi, ^{181}Ta/^{209}Bi, and ^{209}Bi/^{238}U have been measured in the 30–180 MeV energy range using the neutron beam facility at The Svedberg Laboratory in Uppsala. The ^{7}Li(p,n) reaction was employed as a neutron source. The fission fragments were detected by thin-film breakdown counters. Cross sections at specific energies were determined using unfolding techniques with respect to the excitation function and the neutron spectra, the latter obtained from recent measurements and an evaluation. The absolute fission cross sections were obtained using the standard ^{238}U(n,f) cross section. The ^{nat}W(n,f) and ^{181}Ta(n,f) cross sections have been measured for the first time. The results for ^{209}Bi(n,f), ^{nat}Pb(n,f), ^{208}Pb(n,f), and ^{197}Au(n,f) cross sections have been compared with available literature data. A universal easy-to-use parametrization has been suggested for all measured cross sections. The common features of subactinide neutron-induced fission cross sections are found to be similar to those of the proton-induced fission data.

DOI: 10.1103/PhysRevC.70.054603 PACS number(s): 25.85.Ec, 25.40.−h, 28.20.−v, 27.80.+w, 27.70.+q

I. INTRODUCTION

Concepts of accelerator-driven systems (ADS) for incineration of long-lived radioactive waste and energy production (see, e.g., [1]) suggest irradiation of a massive target made of heavy elements by a high-intensity charged particle beam. As a result of nuclear interactions in the target, caused by the primary beam and secondary particles, an intense spallation neutron source is created with an energy distribution extending up to the incident particle energy. This source is intended to feed a subcritical reactor that surrounds the neutron production target and contains the nuclides to be transmuted.

One of the prerequisites for computational modeling of ADS is the availability of evaluated nuclear data for the most important reactions involved. This motivates the choice of nuclides and reactions included in the high priority request list of intermediate-energy nuclear data, which is formulated and periodically updated by Koning *et al.* [2]

The recent high priority list includes requests for nucleon-induced fission cross-section data for a few nuclides considered as prospective spallation target materials. The fission channel contributes to the radioactivity produced in the spallation target, as well as to the chemical and radiological toxicity of the reaction products. For example, fission products in a lead target irradiated by 1.6-GeV protons will contribute 10–15 % to the overall residual activity after one year of cooling [3]. On the other hand, the predictive power of available nuclear reaction models and codes (e.g., LAHET [4], CEM95 [5]) with respect to the description of the fission process is not sufficiently good at present (see, e.g., the studies of Prael [4], Prokofiev *et al.* [5], Duijvestijn *et al.* [6], and a recent comparison of codes for activation yield calculation [7]). For example, the ^{nat}W(p,f) cross section predicted by the LAHET code was found to be about 20 times lower than the experimental result of Ref. [6]. Further progress in nuclear reaction modeling, especially with respect to fission, may therefore lead to significant improvements in ADS performance calculations.

Data on intermediate energy fission cross sections are important also for nuclear theory, e.g., in connection with stud-

*Electronic address: Smirnov@atom.nw.ru
†Electronic address: jan.blomgren@tsl.uu.se
‡Electronic address: Alexander.Prokofiev@tsl.uu.se

ies of the dynamic effects of the nuclear fission process, which reflect the connection between collective and single-particle degrees of freedom in nuclei (see, e.g., [8]).

Proton-induced fission cross sections have been studied extensively (see, e.g., a recent review [9] and references therein). On the other hand, neutron-induced fission experiments above 20 MeV are sparse, mainly because of the lack of suitable neutron sources. In addition, a truly monoenergetic neutron source is not available in this energy domain. Neutron data measurement and processing techniques are therefore unavoidably more complicated than in the case of charged particle beams.

The (n,f) cross-section database is especially poor for subactinide nuclei. The early experiments of Kelly and Wiegand [10], Goldanskiy *et al.* [11], Reut *et al.* [12], and Dzhelepov *et al.* [13] are rather of a qualitative character. The studies of Vorotnikov and Larionov [14] and Vorotnikov [15] are of a high methodological quality, but cover only a narrow energy region near the fission barrier, where the cross sections are extremely small, and therefore only upper limits for cross sections could be obtained in many cases.

During the last decades, a new generation of intermediate energy neutron sources has become available. At a few of them, (n,f) cross-section measurements, in particular, for subactinide nuclei have been included in the experimental programs.

The measurements at the LANSCE neutron facility at Los Alamos National Laboratory were performed by Vonach *et al.* [16] and Staples *et al.* [17,18] in the early 1990s using a parallel-plate ionization chamber. None of these studies has resulted in a final publication. A similar technique was employed in the work of Shcherbakov *et al.* [19] performed at the neutron facility GNEIS at Petersburg Nuclear Physics Institute in Gatchina, and in the work of Nolte *et al.* [20] performed at neutron facilities in Louvain-la-Neuve and Cape Town. A complication in interpreting data of this type is the need to separate subactinide fission events from background of nonfission products, which contribute significantly to the pulse height spectra.

The (n,f) cross-section measurements at the neutron facility in The Svedberg Laboratory (TSL) in Uppsala are part of an experimental program performed in the framework of collaboration between V.G. Khlopin Radium Institute, St. Petersburg, and Uppsala University. Measurements for subactinide nuclei have been performed using two different techniques for fission fragment detection, thin-film breakdown counters (TFBC) [21–26], and a Frisch-gridded ionization chamber [24,27–29].

This paper presents final (n,f) cross-section data for ^{209}Bi, ^{nat}Pb, ^{208}Pb, ^{197}Au, ^{nat}W, and ^{181}Ta, obtained with the TFBC technique. The measurements for natural lead, tungsten, and tantalum are important because these elements are either considered as candidates to the neutron production target material in concepts of future ADS or are already used in existing spallation neutron sources. The doubly magic nucleus ^{208}Pb is included because of its importance for improvements in the theoretical modeling of the fission process. In addition, the ^{197}Au(n,f) cross section was studied in view of its recent application in neutron monitoring [30].

Earlier analyses and preliminary experimental data have been published elsewhere [21–26]. In the present study, the results of further measurements have been added, and the data from our earlier studies have been reanalyzed using new neutron spectrum data [31] and new calculations of energy-dependent detection efficiency corrections [32,33].

II. EXPERIMENTAL APPARATUS AND PROCEDURE

The measurements were performed at the TSL neutron beam facility in Uppsala, using the Gustaf Werner cyclotron to produce neutrons through the ^{7}Li(p,n) reaction. The neutron beam facility and the positioning of the experimental chambers in the beam are described in Sec. II A.

Because of the low beam intensity, inherent for secondary beams, the irradiation position for the most measurements of the present experiment was chosen to be at a short distance from the neutron production target. The incident neutron spectrum is not monoenergetic, but consists of a high-energy peak accompanied by a low-energy tail, which also contributes to the fission reaction rate. To determine the (n,f) cross section at the energy of the peak, one needs to know the fraction of fission events due to that peak. This fraction can be determined using the time-of-flight (TOF) technique. However, in most cases it was not possible to implement the TOF techniques because of the short flight path in combination with the limited time resolution, dominated by duration of the proton beam pulse. Therefore, the fraction of peak fission events was obtained in an iterative unfolding procedure, taking into account relative fission reaction rates at as many incident neutron energies as possible, together with corresponding information on the neutron spectra. The determination of the latter is discussed in Sec. II B.

A severe γ-radiation background was present at the irradiation position chosen for most of the studied reactions. This hampered the use of traditional fission fragment detection techniques and justified the choice of TFBCs, which are sensitive only to particles with specific ionization losses exceeding the detection threshold. The TFBCs and the experimental chambers are described in Sec. II C.

The preparation and characterization of the samples are discussed in Sec. II D. Finally, an outline of the electronics and the data acquisition system is given in Sec. II E.

Most of the studied cross sections were measured relative to the ^{209}Bi(n,f) one. The latter has already been studied in earlier experiments (see, e.g., [21,22]) and has been adopted by IAEA/NDS as a secondary neutron standard [34]. However, further measurements of the ^{209}Bi(n,f) cross section and a new analysis of the earlier results have led to some changes that are discussed in Sec. IV B.

A. Neutron beam facility

An overview of the neutron beam facility is presented in Fig. 1. A comprehensive description of the facility can be found in [35,36], and therefore only the features essential for the present experiment are discussed below.

The proton beam from the Gustaf Werner cyclotron impinged on a 4–15-mm-thick target of lithium, enriched to

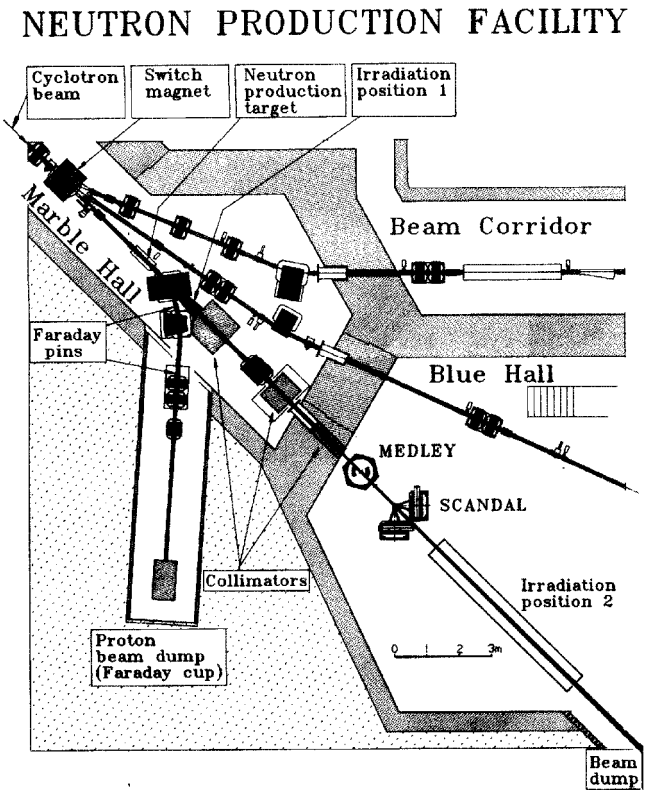

FIG. 1. An overview of the neutron beam facility.

99.98% in ^{7}Li. Downstream of the target, the proton beam was deflected by two magnets into an 8-m-long tunnel, where it was focused onto a water-cooled graphite beam dump. The neutrons produced within a 60-msr cone around 0° passed through a collimating system before reaching the experimental hall at a distance of about 8 m from the production target. The respective area is marked as Irradiation position 2 in Fig. 1. This position was employed in our earlier studies [21,22] and kept in the present work for the ^{209}Bi/^{238}U ratio measurements above 50 MeV, due to a rather large magnitude of the studied cross sections. On the contrary, it was found impractical to measure cross sections of nuclei lighter than Bi and the ^{209}Bi(n,f) cross section below 50 MeV in Irradiation position 2 because of insufficient neutron flux density and small cross-section values. Therefore, in these cases the experimental setup had to be positioned closer to the production target. On the other hand, the neutron field in the irradiation position has to be clean from contamination by primary or scattered protons. In addition, locations close to the 0° direction are preferable, because the production of high-energy neutrons is strongly forward-peaked. The given conditions were satisfied by placing the experimental setup between the proton bending magnet and the first neutron collimator, at a distance of about 2 m from the production target (Irradiation position 1, see Fig. 1). To facilitate simultaneous experiments at the neutron beam line, the setup was placed outside the vacuum tube at an angle of about 4° to the beam axis.

Thus, the TFBC-based chambers with samples of ^{238}U, ^{209}Bi, ^{nat}Pb, ^{208}Pb, ^{197}Au, ^{nat}W and ^{181}Ta were installed in Irradiation position 1, and the chambers with ^{238}U and ^{209}Bi were installed in Irradiation position 2. In addition to count-rate determination, the chamber with ^{238}U was employed as a neutron spectrum sensor (see Sec. II B).

Table I shows thicknesses of the ^{7}Li targets and various energy parameters of the primary proton and secondary neutron beams employed in the different irradiations. In most of the runs, the energy of the protons irradiating the lithium target was measured by time-of-flight techniques with an uncertainty as given in Table I. From this information, the peak neutron energy was calculated using the reaction Q value and the energy loss in the lithium target, estimated using the SRIM code [37].

The proton beam current at the production target was typically 4–6 μA in the 30–100 MeV energy range and 0.3–0.6 μA at the higher energies. The resulting flux density of high-energy peak neutrons at Irradiation position 1 amounted to (3×10^{4})–(3×10^{5}) s^{-1} cm^{-2}, which is a factor of 30–40 more than in Irradiation position 2. This gain was acquired at the price of a limited access to the setup in the course of the experiment and harder requirements on the stability of the detectors with respect to radiation.

The Irradiation position 1 was situated close to the facility for neutron activation studies [36,38]. In Ref. [38], the relative proton (and/or H^{0} atom) contamination in the neutron field was estimated to be as much as 4×10^{-3}. However, in that case most of the protons were produced inside the activation target stack itself. Since the thickness of the stack was much larger than the total amount of material between the neutron production target and any sample in the present experiment, the estimate given above can be considered as an upper limit for the proton or H^{0} atom contamination of the neutron beam that encounters the fission samples.

B. Neutron spectrum

As was mentioned, an unfolding procedure is needed to obtain fission cross sections from the measured reaction

TABLE I. Thicknesses of the ^{7}Li targets and energy parameters of the primary proton and secondary neutron beams.

E_p primary (MeV)	^{7}Li target thickness (mm)	E_p average in the target (MeV)	E_{npeak} average (MeV)
37.96±0.07	4	36.4	34.5
49.2±0.1	4	48.2	46.3
69.1±0.2	4	68.4	66.6
76.4±0.2	4	75.8	73.9
92.1±0.3	4	91.4	89.6
96.8±0.3	4	96.3	94.5[a]
	8	95.6	93.8[a]
114.2±2.0	8	113.1	111.3
136.7±1.0	15	134.7	132.9
148.4±0.6	15	146.4	144.6
177.3±1.0	15	175.2	173.3

[a]The peak neutron energy averaged over the two production modes is 94.1 MeV.

rates. Information on the neutron spectrum at the irradiation position for the various incident neutron energies is therefore required.

A complete set of characterization measurements is not available for the TSL neutron beam. Moreover, the intense background radiation around the production target would hamper the use of most instruments for neutron beam characterization. The present study therefore relies on the following assumptions about the neutron spectrum:

(i) The neutron spectrum at the Irradiation position 1 is a sum of two components. One of them originates directly from the ^{7}Li target. The other is a background arising from interactions of primary protons with the beam transport system, the beam dump, the walls, and other material in the surroundings, with subsequent propagation and slowing-down of secondary neutrons.

(ii) The background component dominates in the low-energy end of the spectrum and vanishes at neutron energies of about 10 MeV [38]. This component could hamper cross-section measurements for reactions with a threshold at lower energy, e.g., ^{238}U(n,f) or ^{235}U(n,f). For subactinide nuclei, with the fission reaction threshold of about 20 MeV or more, the influence of the low-energy background is negligible.

(iii) The energy and angular distribution of neutrons in the first component is defined only by the double-differential cross section (DDX) of the ^{7}Li(p,n) reaction. The basis of this assumption is that no significant amounts of material were present between the neutron production target and the fission samples.

Support for the last assumption is given by the fact that the neutron spectra measured at TSL agree with data from other sources. Figure 2 shows neutron spectra obtained in the course of earlier *n-p* scattering studies at TSL [35,39] at 0° for the peak neutron energies 98, 133, and 160 MeV (shown by filled circles). For comparison, neutron spectra from other facilities are shown as open symbols. The shown spectra were obtained by Byrd and Sailor [40] (triangles) and by Stamer *et al.* [41] (diamonds) at the Indiana University Cyclotron Facility, and by Nakao *et al.* [42] at the RIKEN facility (squares) at peak neutron energies close to the ones in the TSL data. For readability of Fig. 2, the spectra from Refs. [40–42] are shifted by a few MeV in order to match the position of the high-energy peaks. The solid curves represent the neutron spectrum calculations discussed further in the text.

As seen in Fig. 2, the neutron spectrum consists of a high-energy peak and a low-energy tail. The high-energy peak corresponds to the ^{7}Li(p,n) reactions that leave the ^{7}Be nucleus in the ground state or in the first excited state at 0.43 MeV. The low-energy tail is related to excitation of higher states in ^{7}Be and to break-up reactions.

The neutron spectrum calculations were performed in two different ways depending on the peak neutron energy. For peak energies below 45 MeV, interpolated and smoothed experimental data of Byrd and Sailor [40], Baba *et al.* [43], and Schuhmacher *et al.* [44] were used. In cases when the measured spectra do not cover a sufficiently wide range of secondary neutron energies, we used a constant extrapolation to lower energies, which was found to be a reasonable approximation, according to Nolte *et al.* [45]. Above 45 MeV, the

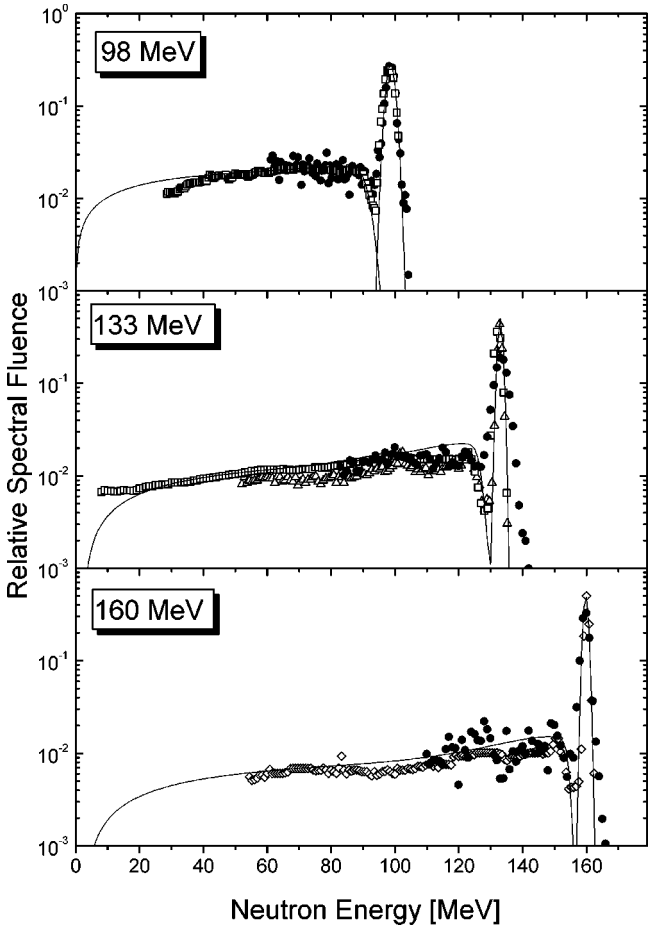

FIG. 2. Neutron spectra from the ^{7}Li(p,n) reaction at 0° for the peak energy of 98, 133, and 160 MeV. The filled circles represent measurements at the TSL neutron facility [35,39] in Irradiation position 2. The open symbols represent data from other facilities: the Indiana University Cyclotron Facility [40,41] (shown as triangles and diamonds, respectively) and the RIKEN facility [42] (shown as squares). The lines represent the neutron spectrum calculations discussed in the text. All spectra are normalized so that the area under the high-energy peak is unity.

calculations employed semiempirical systematics developed in [31], which is based on a phase-space distribution [46] corresponding to the three-body breakup process ^{7}Li$(p,n^{3}$He$)^{4}$He for description of the continuum part of neutron spectra and an empirical correction factor taking into account experimentally observed peculiarities of the high-energy part of the continuum spectra.

As has been mentioned, the experimental setup in Irradiation position 1 was placed at an angle of 4° with respect to the primary proton beam direction. As soon as the production of high-energy neutrons is strongly forward-peaked, the difference between the neutron spectra at 0° and 4° has to be taken into account.

A correction taking into account the decrease in high-energy peak neutron production at 4° relative to 0° was obtained by least-squares fitting to experimentally measured angular distributions from the literature [47–51], with subsequent fitting with respect to incident proton energy. The correction increases from 4% at 38 MeV to 24% at 177 MeV.

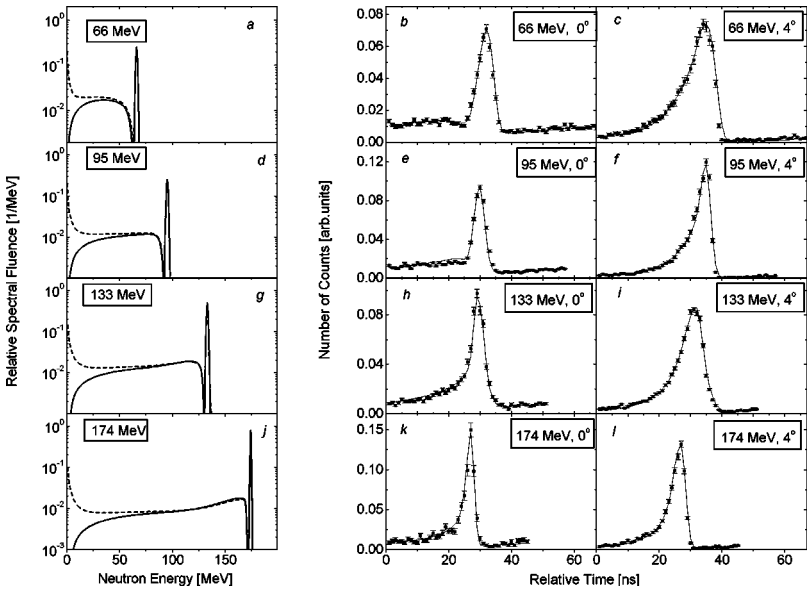

FIG. 3. Calculations of neutron spectra (left panel) for the incident proton energies of 69.1 (a), 96.8 (d), 136.7 (g), and 177.3 MeV (j) used in the present experiment for 0° (solid lines) and 4° (dashed lines). The middle panel (b, e, h, k) represents experimental (symbols) and calculated (lines) distributions of ^{238}U fission events induced by neutrons at a flight path of about 10 m at 0° (in Irradiation position 2). The right panel column (c, f, i, l) represents experimental (symbols) and calculated (lines) distributions of ^{238}U fission events induced by neutrons at a flight path of about 2 m at 4° (in Irradiation position 1).

For continuum neutron production, similar corrections were calculated, which depend on the incident proton energy and the secondary neutron energy. The calculations employed angular distribution data for continuum neutrons from the ^{7}Li(p,n) reaction included in the LA150 library [52]. The latter were obtained with the GNASH code [53], which, in turn, employs the Kalbach representation of the angular distribution [54]. At the 150–175 MeV region, where the LA150 data are not available, an extrapolation was made on the basis of the correction obtained at lower energies.

Validation of the calculations was carried out by means of folding of the calculated spectra with the standard ^{238}U neutron fission cross section [34], followed by conversion to the TOF scale and folding with a function that takes into account the time resolution of the measurement system. Modeled in this way, time distributions of ^{238}U neutron-induced fission events were compared with experimental data obtained both at 0° at Irradiation position 2 and at 4° at Irradiation position 1 simultaneously in the same neutron beam.

In Fig. 3, we show the calculated relative neutron spectral fluence at 0° and 4° for several incident proton energies used in the present experiment, and corresponding calculated and experimental time distributions of fission events in ^{238}U. The spectra at 4° are the sum of the two components mentioned above. The background component is described by a $1/E_n$ distribution. The relative intensity of the background component was fitted to reproduce the experimental distributions of the ^{238}U(n,f) events obtained at Irradiation position 1.

As seen in Fig. 3, the experimental time distributions of the ^{238}U(n,f) events can be successfully reproduced by the model. This ensures adequacy of the chosen representation of the neutron spectra.

C. Fission fragment detectors and experimental chambers

The fission fragments were detected by thin-film breakdown counters (TFBC). A detailed description of the TFBC technique can be found in [55] and references therein; only a brief description is given here. The operation principle of the TFBC is based on the phenomenon of electric breakdown in a MOS structure caused by an ion passing through a thin silicone dioxide layer. The breakdowns are nonshorting, since they lead to vaporization of a small part of the electrode area and leave no conducting path between the electrodes. The features of the TFBCs are threshold behavior, i.e., the insensitivity to light charged particles, neutrons and γ-radiation, real-time operation and good timing properties, easy operation (no high voltage required, no gases, large output signals, which makes preamplifiers unnecessary), compact design, and long-term stability under heavy radiation conditions. The last feature was of primary importance for the present experiment, because of the severe γ-radiation background in the Irradiation position 1.

The choice of detection system design is governed first by the low beam intensity, which necessitates the use of sandwich geometry, i.e., the detector has to be situated as close as possible to the fission sample. The sample-detector sandwich and its mechanical housing constitute an experimental chamber, which is placed in the neutron beam. The amount of material in a chamber along the beam direction is dominated by the thickness of the TFBC (0.3 mm Si). Consequently, the probability of interaction of an incident neutron with the chamber is small, and it is possible to stack several chambers after each other in the neutron beam without any significant influence on the beam characteristics. In this way, relative fission cross sections can be measured using detectors sandwiched with samples of different nuclides and being irradiated by the same neutron beam.

The detection system design is further governed by a trade-off between count rate and time resolution. The latter can be as good as several hundreds of picoseconds for a single TFBC of 1 cm^2 sensitive area. However, to get sufficient statistics, a larger area is required. This can only be achieved at the price of a worsening of the time resolution, because of the unavoidable spread in propagation time of signals originating from different parts of the sensitive area. To achieve both good timing and sufficient count rate, mosaic TFBC arrangements were employed.

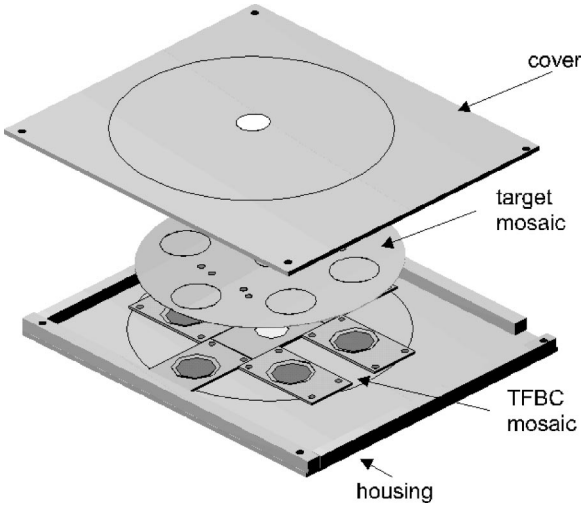

FIG. 4. The design of an experimental chamber.

The design of a single experimental chamber is shown in Fig. 4. The chamber consists of a mosaic arrangement of detectors, a similar arrangement of samples, and a thin mechanical housing. Each chamber contains six TFBCs with a diameter of about 1 cm, placed symmetrically in the plane perpendicular to the neutron beam direction. Six samples of the same nuclide were placed face-to-face to the detectors so that the sensitive area of each detector received fission fragments emitted by the corresponding sample in the forward hemisphere. The distance between the sample and the detector sensitive area (not more than 0.5 mm) could be passed by fission fragments in air without any significant energy loss. Therefore, evacuation of the chamber was not necessary. Upstream and downstream of the sample-detector sandwiches, the incident neutron beam passed through the entrance and exit windows, respectively, which were made of 0.2-mm-thick aluminum foils.

The entire experimental setup consisted of six to nine chambers described above, depending on the specific irradiation. The chambers were stacked along the neutron beam direction, so that each set of sample-detector sandwiches was exposed to virtually the same neutron fluence. Each chamber was equipped either with samples of one of the studied nuclides (^{209}Bi, ^{nat}Pb, ^{208}Pb, ^{197}Au, ^{nat}W, and ^{181}Ta) or with the monitor samples (^{238}U or ^{209}Bi).

All detectors have common bias voltage and a common signal output. Typically, the mosaic arrangement provides an output pulse height of about 1–2 V and a time resolution of about 2 ns (full width at half maximum).

D. Fission samples

The samples were prepared by deposition on circular 0.1-mm-thick aluminum backings of 1 cm^2 area. In all cases, the area of the sample exceeded the sensitive area of the respective TFBC. Therefore, the latter defined the effective area of the sandwich.

The employed deposition techniques, the chemical composition, and the thickness of the samples are listed in Table II. The samples of ^{208}Pb and ^{238}U had an isotopic purity of 98.7% and 99.999%, correspondingly, while the other samples contained either monoisotopic elements (^{209}Bi, ^{197}Au, ^{181}Ta) or natural isotopic compositions (^{nat}Pb, ^{nat}W).

TABLE II. Characteristics of the fission samples.

Target	Chemical composition	Deposition technique	Average sample thickness (mg/cm^2)
^{238}U	$^{238}U_3O_8$	multiple smearing	0.1–1.1
^{209}Bi	^{209}Bi	vacuum evaporation	1.1–3.1
^{nat}Pb	^{nat}Pb	vacuum evaporation	1.1–2.4
^{208}Pb	^{208}Pb	vacuum evaporation	1.3–2.4
^{197}Au	^{197}Au	vacuum evaporation	2.8
^{nat}W	$^{nat}WO_3$	vacuum evaporation	2
^{181}Ta	^{181}Ta	magnetron evaporation	0.5–1.2

The thickness of the samples was determined by Rutherford backscattering spectroscopy (in the case of the subactinide targets), by direct α-spectroscopy (in the case of ^{238}U), and/or by direct weighing of the sample backing before and after deposition of the material.

Since the expected fission cross sections of the studied subactinide nuclei were a few orders of magnitude smaller than those of actinide nuclei, the actinide contamination of the samples was checked using the following techniques:

(i) Direct α-spectroscopy measurements using semiconductor detectors.

(ii) α-activity measurements using low-background nuclear track detectors [56].

(iii) Irradiation by a 21-MeV neutron beam. Because of the very low fission cross sections of the studied nuclei at this energy, virtually all detected fission events could be attributed to actinide contaminants.

In addition, an upper limit of the contamination could be deduced from the TOF spectra of fission events accumulated during the irradiations. The results obtained with the listed techniques were mutually compatible. The obtained upper limit for the relative abundance of actinide nuclei in the subactinide samples amounted to 10^{-5}–10^{-6} depending on the studied nuclide.

E. Electronics and data acquisition system

A schematic view of the electronics and the data acquisition system is shown in Fig. 5. Since the signals from the TFBCs are large (see Sec. II C), they could be fed into a fast multichannel leading-edge discriminator without any preceding amplification. The discrimination level could always be set so that virtually all detector pulses were accepted. The logical signals from the discriminator were summed and fed into the start input of a TDC. A pulse, phase-locked to the cyclotron RF, served as the stop signal for the TDC. In addition, the discriminated signal from each fission chamber was recorded by a scaler, and this information was used in the analysis to separate the TOF spectra of fission events from the different chambers. The TOF spectra and the count-

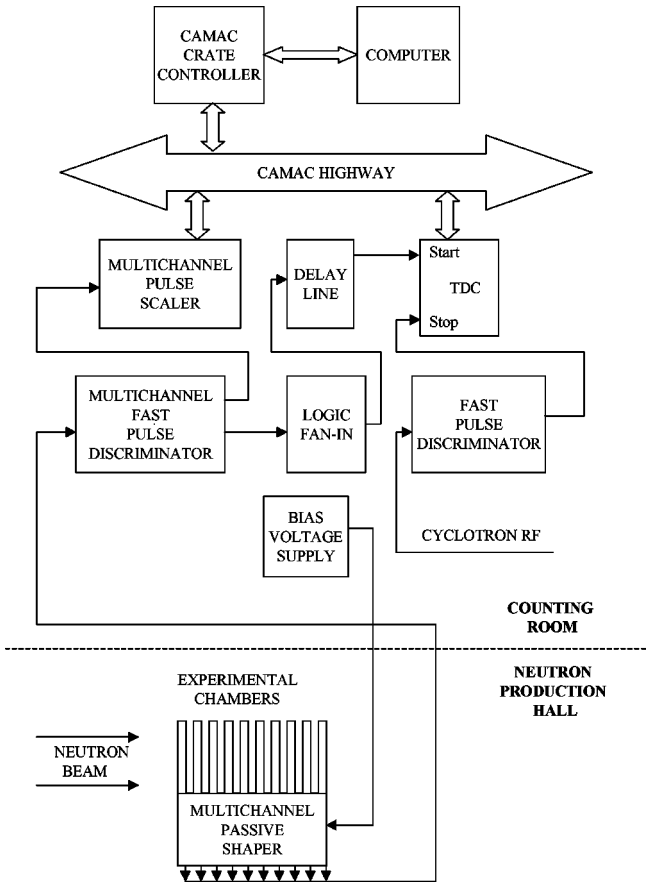

FIG. 5. A schematic view of the electronics and the data acquisition system.

rate data were stored in a computer on an event-by-event basis and could be inspected on-line.

As discussed above, in most cases it was not possible to fully separate the high-energy peak fissions from those of the low-energy tail using TOF techniques. Nevertheless, TOF techniques were useful for rejection of intrinsic detector background events, as well as of those from spontaneous fission of contaminating nuclides. In addition, inspection of the low-energy part in the TOF spectra allowed us to check that no significant actinide contamination was present in the subactinide fission samples.

III. DATA ANALYSIS

A. Fission cross-section ratio

The number of detected fission events per unit incident energy, induced by neutrons with an arbitrary spectrum, is

$$n_f(E) = \rho S_{sample} \varphi_n(E) \sigma_f(E) \varepsilon(E), \tag{1}$$

where E is the incident neutron energy, ρ is the number of nuclei in the sample per unit area, S_{sample} is the sample area (1 cm^2 in our case), $\varphi_n(E)$ is the spectral density of the neutron fluence, $\sigma_f(E)$ is the fission cross section, and $\varepsilon(E)$ is the detection efficiency, defined as the ratio of the number of detected fragments to the number of fissions in the sample.

The efficiency, as defined above, accounts for the anisotropy of the fragment angular distribution in the laboratory frame, as well as for loss of fragments due to a possible mismatch between the area of the sample and the sensitive area of the TFBC, S_{TFBC}. Since each TFBC was exposed to a calibration sample of 1 cm^2 area containing ^{252}Cf, the difference between S_{sample} and individual S_{TFBC} was automatically taken into account, and the detection efficiency for fragments of neutron-induced fission can be expressed as

$$\varepsilon(E) = k_\varepsilon(E) \varepsilon^{\mathrm{Cf}}, \tag{2}$$

$$\varepsilon^{\mathrm{Cf}} = n_{sf}/a_{sf}, \tag{3}$$

where n_{sf} is the count rate of fragments from spontaneous fission, a_{sf} is the spontaneous fission activity of the ^{252}Cf sample, and

$$k_\varepsilon^X(E) = \frac{\varepsilon_{ac}^X(E)}{\varepsilon_{ac}^{\mathrm{Cf}}}, \tag{4}$$

where $\varepsilon_{ac}^{\mathrm{Cf}}$ and ε_{ac}^X are the calculated absolute detection efficiencies of the TFBC and a sample of unit area for the fragments of ^{252}Cf spontaneous fission and induced fission of nuclide X, respectively.

Combining Eqs. (1) and (2) gives

$$n_f(E) = \langle \rho \varepsilon^{\mathrm{Cf}} \rangle k_\varepsilon^X(E) \varphi_n(E) \sigma_f(E), \tag{5}$$

where $\langle \rho \varepsilon^{\mathrm{Cf}} \rangle$ is the product of the values ρ and $\varepsilon^{\mathrm{Cf}}$ averaged over all sandwiches for the corresponding fission chamber. Integration over the entire incident neutron spectrum gives the total number of detected fissions,

$$N_f = \langle \rho \varepsilon^{\mathrm{Cf}} \rangle \int_0^{E_{\max}} k_\varepsilon^X(E) \varphi_n(E) \sigma_f(E) dE. \tag{6}$$

The number of fissions induced by the high-energy peak neutrons in the quasimonoenergetic spectrum can be obtained by integration over the peak only. Since the relative efficiency and the fission cross section vary slowly with energy, they can be replaced by the values corresponding to the peak energy E_0, i.e., $k_{\varepsilon 0} = k_\varepsilon^X(E_0)$ and $\sigma_{f0} = \sigma_f(E_0)$. Thus,

$$N_{fpeak} = \langle \rho \varepsilon^{\mathrm{Cf}} \rangle k_{\varepsilon 0} \sigma_{f0} \Phi_{n0}, \tag{7}$$

where Φ_{n0} is the fluence of the high-energy peak neutrons. The fraction of detected fissions due to the peak, $k_{peak} = N_{fpeak}/N_f$, can be deduced from Eqs. (6) and (7),

$$k_{peak} = \frac{\sigma_{f0} k_{\varepsilon 0} \Phi_{n0}}{\int_0^{E_{\max}} k_\varepsilon(E) \varphi_n(E) \sigma_f(E) dE}. \tag{8}$$

Combining Eqs. (6) and (8) gives the peak fission cross section

$$\sigma_{f0} = \frac{N_f k_{peak}}{\langle \rho \varepsilon^{\mathrm{Cf}} \rangle k_{\varepsilon 0} \Phi_{n0}}. \tag{9}$$

Finally, the fission cross-section ratio measured with a pair of sandwich arrangements X and Y, stacked one after the other in the neutron beam, is

$$\frac{\sigma_{f0(X)}}{\sigma_{f0(Y)}} = \frac{N_{f(X)}\langle \rho\varepsilon^{\mathrm{Cf}}\rangle_{(Y)} k_{peak(X)} \varepsilon^{X}_{ac}(E_0) R^2_{(X)}}{N_{f(Y)}\langle \rho\varepsilon^{\mathrm{Cf}}\rangle_{(X)} k_{peak(Y)} \varepsilon^{Y}_{ac}(E_0) R^2_{(Y)}}, \qquad (10)$$

where R is the distance between the production target and the chamber. The quantities $\langle \rho\varepsilon^{\mathrm{Cf}}\rangle$, R, and N_f were obtained in direct measurements for the respective chambers. The latter quantity was corrected for intrinsic detector background on the basis of the obtained TOF spectra of fission events. The determination of the remaining parameters in Eq. (10), $\varepsilon^{X}_{ac}(E)$ and k_{peak}, is discussed in Secs. III B and III C, respectively.

B. Determination of the detection efficiency

The detection efficiency of a TFBC in sandwich geometry cannot be directly measured for a particle source with unknown intensity and arbitrary angular-energy distribution, since the counting characteristics (efficiency versus bias voltage) does not have a plateau corresponding to detection of all fragments that reach the sensitive area. Instead, a model calculation has to be employed, and the parameters of the model have to be determined in dedicated measurements for each specific detector (or for a group of detectors with similar properties), operated at a given bias voltage.

A model and a computer code for calculation of the TFBC detection efficiency have been described in our earlier report [32]. A thorough description is going to be published elsewhere [33]. A brief outlook of the model and the code is given below.

The model and the code are based on semiempirical dependences of the detection threshold voltage on specific energy losses of fission fragments in SiO_2 and on the incident angle of fission fragments to the sensitive surface of the detector [57]. The code makes use of Monte Carlo techniques to model the process of detection for fission fragments from either spontaneous or nucleon-induced fission. The model takes into account angular anisotropy of fission and transferred longitudinal momentum that define angular distributions of fission fragments. A change in fission fragment kinetic energy due to the transferred momentum is taken into account, as well as the energy losses of fission fragments in the sample material and their dependence on the fragment angular distribution.

The input data of the code include the following.

(i) Charge, mass, and kinetic energy distributions of fission fragments, taking into account the emission of prefission neutrons. In the case of the $^{238}\mathrm{U}(n,f)$ reaction, experimental data of Zoller [58] were employed. At present, data of this type for neutron-induced fission of subactinide nuclei remain unmeasured. Therefore, we used symmetric Gaussian-shaped charge and mass distributions that are typical for similar fissioning systems formed in reactions of charged particles with subactinide nuclei [59,60].

(ii) The total kinetic energy of fission fragments from the systematics of Viola *et al.* [61].

(iii) Energy-range data [62] for fission fragments in sample materials and SiO_2.

(iv) Energy-dependent data on fission anisotropy and longitudinal linear momentum transferred to fissioning nuclei, from systematics developed in [26].

The code was verified using experimental results for TFBC detection efficiency for spontaneous fission of ^{252}Cf as well as for proton- and neutron-induced fission of different nuclides [32,33]. The estimated error of the calculated efficiency is not more than 5% for the whole range of the projectile energies.

The calculated absolute efficiency is plotted in Fig. 6 versus incident neutron energy for the samples of $^{238}U_3O_8$, ^{209}Bi, ^{nat}Pb, ^{208}Pb, ^{197}Au, $^{nat}WO_3$, and ^{181}Ta samples employed in the present study. The values given in the graphs represent the sample thickness, averaged over the corresponding mosaic arrangement. As can be seen, the efficiency for a given sample material and neutron energy decreases with the sample thickness, which reflects the increase in the fraction of fragments escaping detection due to the energy loss in the sample. The results for different sample materials show a decrease in efficiency from the heaviest considered nuclides, ^{238}U and ^{209}Bi, to the lightest, ^{181}Ta, which is mainly governed by a decrease in the average fragment kinetic energy. A special case is the samples of tungsten trioxide. The presence of oxygen atoms in the sample material increases its stopping power and, therefore, diminishes the detection efficiency. This effect is not so pronounced for

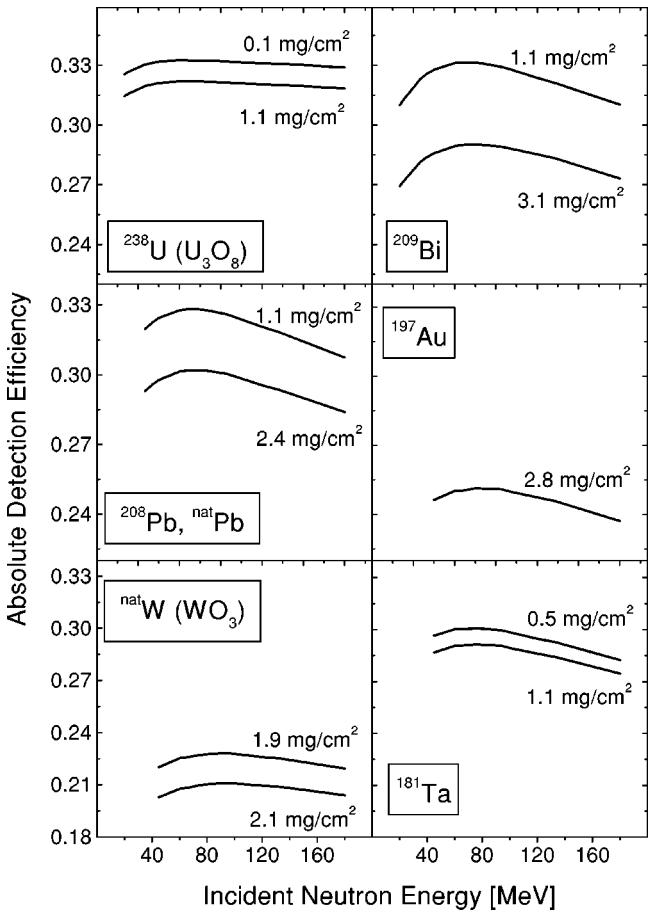

FIG. 6. The calculated fission fragment detection efficiency for the TFBC and a sample of the unit area, versus incident neutron energy.

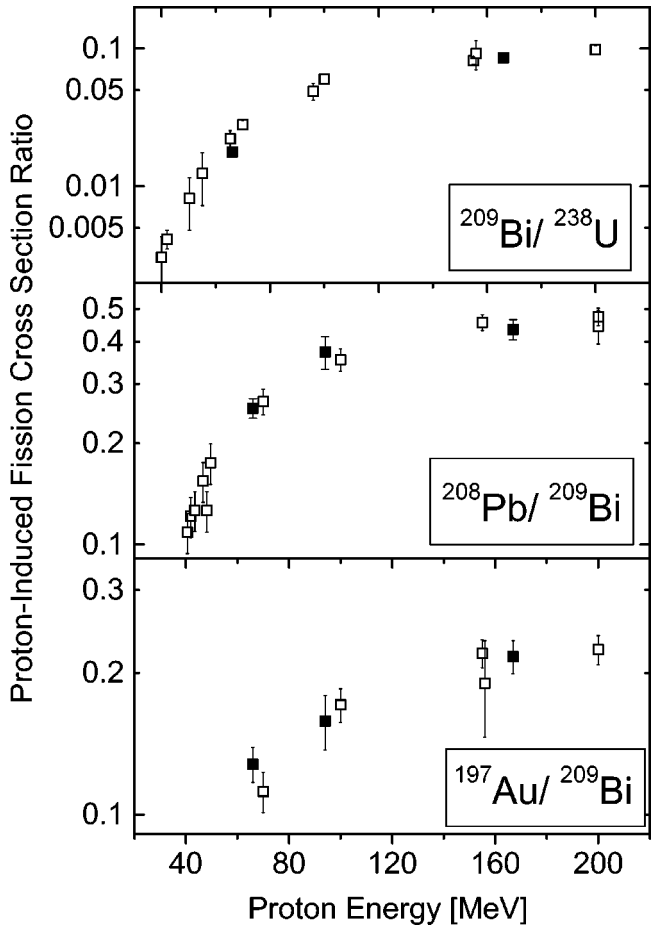

FIG. 7. Energy dependences of the ^{209}Bi/^{238}U, ^{208}Pb/^{209}Bi, and ^{197}Au/^{209}Bi proton-induced fission cross-section ratios. The filled symbols represent the results of the present work. The open symbols represent results extracted from a compilation of literature experimental data [9].

the $^{238}U_3O_8$ samples because of their relatively small thickness.

The same model and code were employed in processing of experimental data on proton-induced fission cross sections [32], obtained at the broad proton beam facility at TSL [63] with the same detector arrangement as in the present study. The relative (p,f) cross-section results are presented in Fig. 7 together with data of other authors from a review [9]. As seen in Fig. 7, the data of our work [32] agree with the literature data within the uncertainty limits. This provides an additional check of the developed model and code for detection efficiency calculations.

C. Determination of the fraction of peak fission events

To determine the fraction of peak fission events, k_{peak}, defined in Eq. (8), two different methods were employed.

(i) For the ^{238}U(n,f) reaction, we used TOF techniques supplemented by model calculations (see Sec. III C 1).

(ii) For the other studied reactions, an iterative unfolding procedure was used (see Sec. III C 2).

Uncertainties in determination of the factor k_{peak} are discussed in Sec. III C 3.

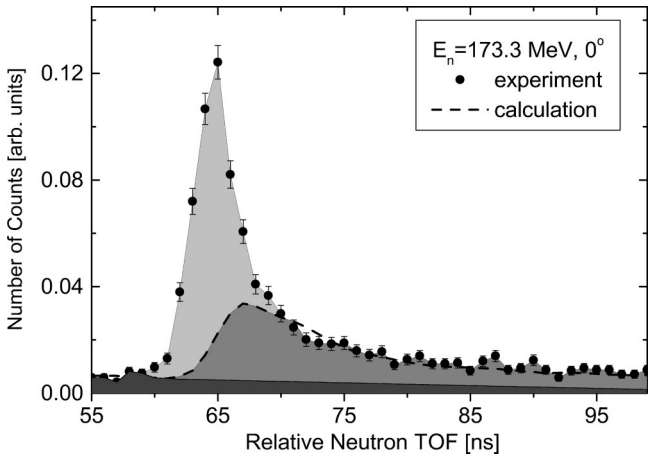

FIG. 8. The TOF spectrum of ^{238}U neutron-induced fission events induced by neutrons from the 7Li(p,n) reaction with the peak neutron energy of 173.3 MeV and its decomposition. The symbols represent experimental data of the present work. The dashed curve represents calculated TOF distribution of fission events induced by the continuum part of the neutron spectrum. The light-gray area represents fission events induced by high energy peak neutrons. The events in the dark-gray area originate from high energy continuum neutrons with energy above about 60 MeV. The black area corresponds to fission events induced by "wrap-around" neutrons with energy lower than 60 MeV, which are produced by previous proton beam micropulses.

1. Determination of the factor k_{peak} using TOF techniques

Distributions of ^{238}U fission events on the relative neutron TOF were measured using an experimental chamber placed at a flight path of about 10 m at 0°. An exemplary distribution, shown in Fig. 8, was obtained in irradiation by neutrons with the peak energy of 173.3 MeV. The light-gray area in the spectrum corresponds to fission events induced by the high-energy peak neutrons. Thus, the sought factor is a ratio between the light-gray area and the total area under the spectrum.

Fission events in the dark-gray area in Fig. 8 originate from high-energy continuum neutrons with energy above about 60 MeV. The black area corresponds to fission events induced by "wrap-around" neutrons with energy lower than 60 MeV, which are produced by previous proton beam micropulses. In order to estimate and subtract the last two components, the studied TOF distribution was modeled. Input data for the model calculations included the standard ^{238}U(n,f) cross section [34] and the incident neutron spectra. The latter were either calculated according to the systematics [31] or interpolated or extrapolated from the experimentally measured spectra [35,39–44]. The resulting values of the factor k_{peak} are given in Table III.

Similar TOF spectra were obtained for ^{209}Bi fission events at the same flight path of about 10 m. However, the statistics was not sufficient for the spectrum decomposition procedure. The decomposition was not possible either for the nuclides lighter than Bi, because those measurements were performed only at a short flight path. Therefore, for all subactinide nuclei, we had to skip the TOF information and to employ an

TABLE III. Correction factor k_{peak} for the $^{238}U(n,f)$ and $^{209}Bi(n,f)$ reactions for neutron spectra at 0°.

E_{npeak} (MeV)	$k_{peak}(^{238}U)$	$k_{peak}(^{209}Bi)$
34.5	0.55±0.02	0.98±0.02
34.5	0.43±0.02[a]	0.97±0.02[a]
34.5	0.35±0.02[b]	0.96±0.02[b]
46.3	0.44±0.01	0.95±0.03
66.6	0.37±0.01	0.82±0.01
73.9	0.36±0.01	0.81±0.01
89.6	0.37±0.01	0.73±0.02
94.1	0.37±0.01	0.71±0.02
111.3	0.37±0.01	0.67±0.02
132.9	0.39±0.01	0.64±0.01
144.6	0.35±0.01	0.61±0.01
173.3	0.42±0.01	0.63±0.01

[a]Correction factor at the position of the facility for activation studies [36,38] at about 1°.
[b]Correction factor at the irradiation position 1 at about 4°.

iterative unfolding procedure discussed in the subsequent subsection.

2. Determination of the factor k_{peak} using the iterative unfolding procedure

The unfolding procedure in the present work is similar to the one that was implemented in an analysis of neutron-induced single-event upsets performed by Johansson *et al.* [64]. However, the present study makes use of a more advanced description of the incident neutron spectrum (see Sec. II B). The procedure is described below for the $^{209}Bi(n,f)$ reaction.

To get a first estimate of the factor k_{peak}, we constructed a trial input cross section $\sigma_f(^{209}Bi) = \sigma_f(^{238}U)N_f(^{209}Bi)/N_f(^{238}U)$, where $\sigma_f(^{238}U)$ is the standard $^{238}U(n,f)$ cross section [34], and N_f denotes the fission count rate for a given nuclide, integrated over the whole corresponding TOF spectrum. The trial cross section, fitted by a smooth curve, together with the experimental [35,39–44] or calculated [31] neutron spectra at 0° and the relative detection efficiency, were used to calculate the factor k_{peak} for each beam energy employed in the study. Then, the $^{209}Bi/^{238}U$ fission cross-section ratios were calculated according to Eq. (10), using the factors $k_{peak}(^{209}Bi)$ obtained as described above and the factors $k_{peak}(^{238}U)$ obtained with TOF techniques as described in Sec. III C 1. Finally, multiplication of the obtained $^{209}Bi/^{238}U$ ratios and the standard $^{238}U(n,f)$ cross section [34], with subsequent smoothing of the energy dependence, resulted in the new trial $^{209}Bi(n,f)$ cross section. The procedure was repeated until convergence was reached. Usually, two iterations were sufficient. The correction in the last iteration did not exceed 0.5%. The resulting values of $k_{peak}(^{209}Bi)$ are presented in Table III.

A similar procedure was employed for the studied reactions with the nuclei lighter than Bi. In this case, only the calculated neutron spectra at 4° were used. The factor k_{peak} for the monitor $^{209}Bi(n,f)$ reaction was calculated using the parametrization of the experimental cross section obtained in the present work (see Sec. IV D). In all cases, the result was found to be independent of the initially assumed cross section.

3. Uncertainties in the factor k_{peak}

The uncertainties in the factor k_{peak} amounted to 2–3 % depending on the neutron energy and the studied reaction. In the case of the $^{238}U(n,f)$ reaction, the uncertainties reflect statistical errors in the TOF spectra, as well as uncertainties in the input data of the model calculations and ambiguities in the spectrum decomposition procedure. For the other reactions, the uncertainties reflect the ones in the neutron spectrum data, which served as input in the unfolding procedure.

The studied excitation functions of the subactinide fission reactions have rather similar shapes, and therefore it is possible to further suppress the contribution that comes from the determination of the factor to the total uncertainty in the relative cross-section measurement. For this purpose, we studied sensitivity of the ratio $k_{peak}(X)/k_{peak}(^{209}Bi)$ (where X denotes the studied target nuclide) to the neutron spectrum data used as input in the unfolding procedure. Using different experimental [42,43] and calculated [31] neutron spectra, we estimated that the variation in the ratio $k_{peak}(X)/k_{peak}(^{209}Bi)$ did not exceed 1% for any studied nuclide.

IV. EXPERIMENTAL RESULTS

A. The $^{209}Bi(n,f)$ cross section

The $^{209}Bi/^{238}U$ ratios measured in the present work were converted into absolute values using the standard $^{238}U(n,f)$ cross section taken from the work of Carlson *et al.* [34]. The $^{209}Bi(n,f)$ cross sections obtained in our earlier studies [21,22] have been revised using the new approach to the fission fragment detection efficiency and the factor k_{peak}, and have been taken into account in processing of the results of the present work. The results are presented in Table IV.

TABLE IV. Neutron-induced fission cross section of ^{209}Bi.

E_{npeak} (MeV)	$^{209}Bi(n,f)/^{238}U(n,f)$ cross-section ratio	$^{209}Bi(n,f)$ cross section (mb)
34.5	$(1.90\pm0.20)\times10^{-4}$	0.311±0.034
46.3	$(1.05\pm0.10)\times10^{-3}$	1.71±0.17
66.6	0.0054±0.0005	8.42±0.81
73.9	0.0082±0.0007	12.6±1.2
89.6	0.0133±0.0012	19.2±1.9
94.1	0.0157±0.0014	22.4±2.2
111.3	0.0247±0.0027	33.5±3.9
132.9	0.0307±0.0027	40.5±4.1
144.6	0.0335±0.0031	44.2±4.7
160.0	0.0415±0.0038	54.6±5.7
173.3	0.0417±0.0040	54.9±5.9

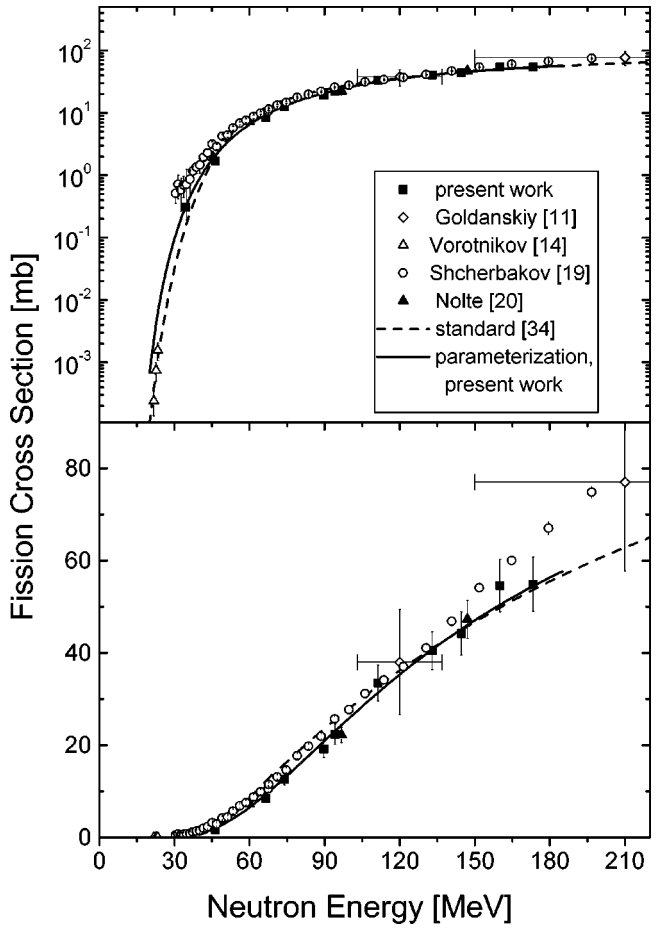

FIG. 9. Absolute neutron-induced fission cross sections of ^{209}Bi. The scale of the vertical axis is logarithmic and linear in the upper and lower panels, respectively, in order to show the behavior of the cross section in the different energy regions.

The uncertainties in the absolute fission cross sections given in Table IV include the uncertainty in the standard ^{238}U(n,f) cross section [34], which amounts to 2–5 % depending on the neutron energy. The uncertainties in the relative measurements are discussed in Sec. IV B for all studied reactions together.

Our data on the ^{209}Bi(n,f) cross sections are shown in Fig. 9 together with earlier data of Vorotnikov *et al.* [14], as well as with recent data of Nolte *et al.* [20] and Shcherbakov *et al.* [19]. In order to avoid complicating the figure, we do not show data of Staples *et al.* [17,18], because they are very close to the results of Shcherbakov *et al.* [19].

As seen in Fig. 9, our data agree within the uncertainties with the data of Shcherbakov *et al.* [19] in the neutron energy range above about 95 MeV. However, there is a systematic deviation at lower energies. The latter data systematically exceed our data in the energy range from 30 to about 95 MeV. The deviation is most clearly seen in the energy region below about 50 MeV. This could possibly be explained by a well-known problem of nonfission background in ionization chambers discussed frequently in the literature (see, e.g., [29]). The data of Nolte *et al.* [20] are in good agreement with our data in the entire neutron-energy range of their measurements.

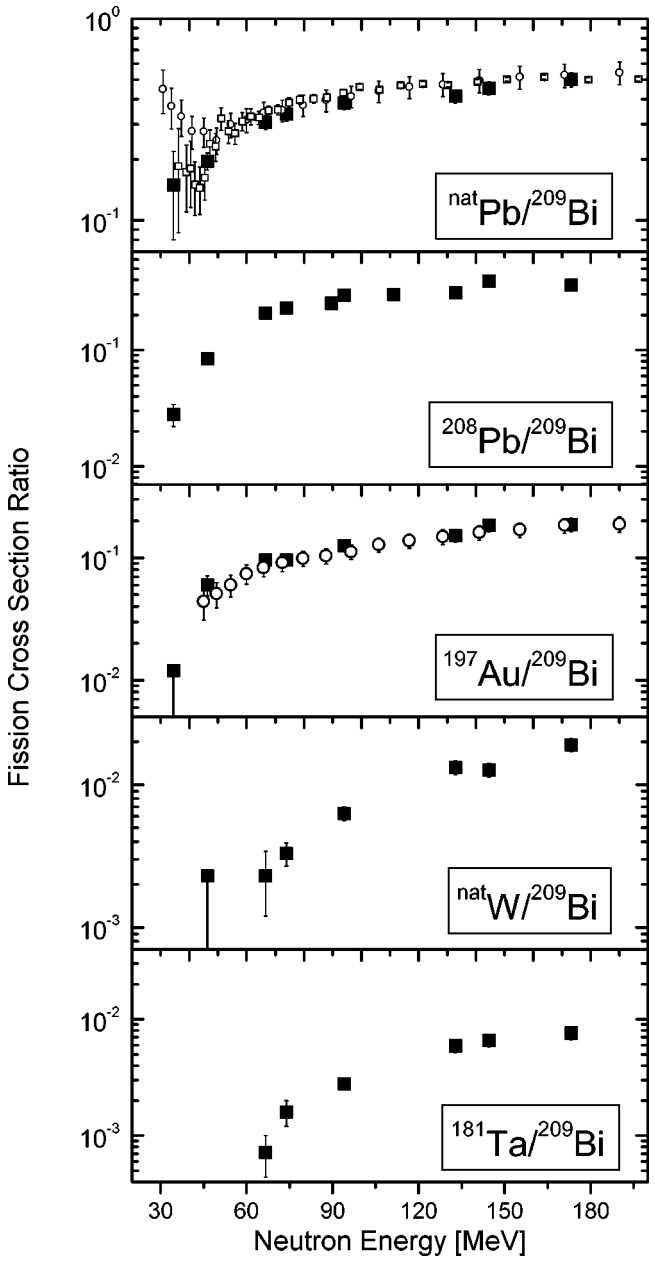

FIG. 10. Neutron-induced fission cross-section ratios ^{nat}Pb/^{209}Bi, ^{208}Pb/^{209}Bi, ^{197}Au/^{209}Bi, ^{nat}W/^{209}Bi, and ^{181}Ta/^{209}Bi versus incident energy. The results of the present study are shown as filled squares. The open squares and circles show data deduced from the results of Shcherbakov *et al.* [19] and Staples *et al.* [17,18], respectively.

The ^{209}Bi(n,f) cross section has been adopted as standard in 1996 [34], and the corresponding parametrization is shown in Fig. 9 as a dashed line. However, in the recommendations of the IAEA [34], it was noted that the available experimental database was not sufficient, and new experimental results were needed in order to make a more accurate parametrization. Such new parametrization is suggested in the present work (see Sec. IV D) and shown in Fig. 9 as a solid line. A comparison of the recent parametrization with the standard one [34] shows considerable differences. The standard fit lies about 40% lower than the new one in the

TABLE V. Relative neutron-induced fission cross sections for the nuclei lighter than Bi.

E_{npeak} (MeV)	Fission cross-section ratios $^{nat}Pb/^{209}Bi$	$^{208}Pb/^{209}Bi$	$^{197}Au/^{209}Bi$	$^{nat}W/^{209}Bi$	$^{181}Ta/^{209}Bi$
34.5	0.15±0.07	0.028±0.006	<0.012		
46.3	0.197±0.019	0.084±0.007	0.060±0.011	<0.0023	
66.6	0.306±0.023	0.208±0.016	0.096±0.011	0.0023±0.0011	(7.2±2.8)10⁻4
73.9	0.336±0.026	0.230±0.018	0.096±0.010	0.0033±0.0006	0.0016±0.0004
89.6		0.252±0.020			
94.1	0.383±0.028	0.297±0.023	0.126±0.013	0.0063±0.0007	0.0028±0.0003
111.3		0.301±0.026			
132.9	0.414±0.031	0.310±0.024	0.151±0.017	0.0132±0.0015	0.0059±0.0007
144.6	0.452±0.034	0.39±0.03	0.184±0.021	0.0127±0.0014	0.0066±0.0008
173.3	0.50±0.04	0.36±0.03	0.187±0.023	0.019±0.002	0.0076±0.0009

20–45 MeV energy range, and about 20% higher between 50 and 90 MeV. For energies above 90 MeV, the standard fit lies not more than 10% higher than the new one. The mentioned differences, however, are within the declared uncertainties for the standard parametrization [34].

B. Relative cross sections for the nuclei lighter than Bi

The fission cross-section ratios obtained in this work for the nuclei lighter than Bi are given in Table V and are shown in Fig. 10 together with data deduced from the previously reported results of Staples *et al.* [17,18] for $^{209}Bi/^{235}U$, $^{nat}Pb/^{235}U$, and $^{197}Au/^{235}U$ fission cross-section ratios and Shcherbakov *et al.* [19] for $^{209}Bi/^{235}U$ and $^{nat}Pb/^{235}U$.

The following uncertainties for the relative fission cross sections were considered.

(i) Sample thickness determination (2–7 % depending on specific sample arrangement).

(ii) Counting statistics in the ^{252}Cf calibration (1–2 % depending on specific detector arrangement).

(iii) Calculation of relative detection efficiency (5%).

(iv) Variations of neutron beam intensity, sample thickness, and detection efficiency from one sandwich to another in a mosaic arrangement ($\leqslant$0.3% in most cases, 0.6% in the worst case).

(v) In-beam counting statistics and subtraction of background (0.5–50 % depending on neutron energy and specific detector-sample arrangement).

(vi) Determination of the fraction of peak fission events k_{peak} ($\leqslant$4% for the $^{209}Bi/^{238}U$ ratio and $\leqslant$1% for the other ratios, see Sec. III C 3).

The total uncertainties of the obtained cross-section ratios given in Tables IV and V amount typically to 10–15 %, depending on the studied reaction and neutron energy. At the lowest energy points, the total uncertainties are dominated by statistical errors and amount to 20–50 % depending on the studied reaction.

A number of other possible error sources were considered. The direct measurements of the irradiation geometry gave uncertainty contributions of not more than 0.1%. The influence on the results caused by proton (and/or H^0 atom) contamination in the neutron field was estimated using the (p,f)

TABLE VI. Absolute neutron-induced fission cross sections.

E_{npeak} (MeV)	Fission cross section ^{nat}Pb (mb)	^{208}Pb (mb)	^{197}Au (mb)	^{nat}W (mb)	^{181}Ta (mb)
34.5	0.047±0.021	0.0087±0.0021	<0.0038		
46.3	0.336±0.044	0.143±0.018	0.103±0.019	<0.004	
66.6	2.58±0.30	1.75±0.21	0.81±0.12	0.020±0.010	0.0061±0.0024
73.9	4.24±0.47	2.90±0.33	1.20±0.17	0.041±0.008	0.020±0.005
89.6		4.8±0.5			
94.1	8.6±1.0	6.6±0.8	2.81±0.39	0.141±0.020	0.063±0.009
111.3		10.1±1.3			
132.9	16.8±1.7	12.6±1.3	6.1±0.9	0.53±0.08	0.24±0.04
144.6	20.0±2.3	17.3±2.0	8.1±1.2	0.56±0.08	0.29±0.05
173.3	27.5±3.7	19.9±2.7	10.3±1.6	1.04±0.15	0.42±0.07

systematics [9] and was found to be negligible. The attenuation of the neutron beam along the stack of the experimental chambers in Irradiation position 1 was measured directly with a pair of chambers with ^{209}Bi samples placed upstream and downstream of the other chambers in the stack, and no significant effect was found. No correction was necessary for neutron-induced and spontaneous fission of contaminating heavier nuclides in the subactinide samples. The calibrations with a ^{252}Cf sample were performed before and after each experimental period, in order to reveal possible changes in the detector efficiency and sensitive area. In addition, possible drifts of the detector parameters during the beam exposure were checked by monitoring the respective count-rate ratios. In all cases, no effect was found outside the statistical uncertainties.

In many cases, the presented data were determined with samples of different thicknesses and obtained during different experimental periods. In all cases, the results agreed within the uncertainties, and therefore the respective weighted average values were adopted as final.

The presented upper limits of the cross sections were obtained using the prescriptions of Schmidt *et al.* [65] for analysis of data with small counting statistics.

C. Absolute cross sections for the nuclei lighter than Bi

The relative fission cross sections for the nuclei lighter than Bi were converted into absolute ones using the revised set of the experimental ^{209}Bi(n,f) cross-section data given in Table IV. The resulted absolute cross sections are given in Table VI and shown in Fig. 11 together with our earlier data for ^{208}Pb [21,22], as well as with earlier data of Reut *et al.* for ^{197}Au and ^{nat}Pb [12], Dzhelepov *et al.* for ^{nat}W [13], Vorotnikov *et al.* [14], Shcherbakov *et al.* [19], and Nolte *et al.* [20] for ^{nat}Pb, Vorotnikov [15], and Staples *et al.* [17,18] for ^{197}Au. The given uncertainties of our results include those of the new data set for the ^{209}Bi(n,f) cross section (see Table IV). The absolute data of Staples *et al.* shown in Fig. 11 were deduced by multiplying the ^{197}Au/^{235}U ratios [17,18] with the standard ^{235}U(n,f) cross section [34].

D. Cross-section parametrizations

Parametrizations of the absolute (n,f) cross sections of subactinide nuclei suggested in the present work are based on our data presented in Tables IV and VI, together with the data of Nolte *et al.* [20] for ^{209}Bi and ^{nat}Pb. The following universal parametrization of the cross section σ_f versus neutron energy E_n is suggested:

$$\sigma_f(E_n) = P_1 \exp[-(P_2/E_n)^{P_3}], \tag{11}$$

where P_1, P_2, and P_3 are fitting parameters that depend on the target nuclide. The values of the parameters, obtained by the least-squares method, are given in Table VII. The parametrizations are shown as solid lines in Figs. 9 and 11.

V. DISCUSSION

The first published measurement results are presented for the ^{nat}Pb, ^{197}Au, ^{nat}W, and ^{181}Ta(n,f) cross sections. The

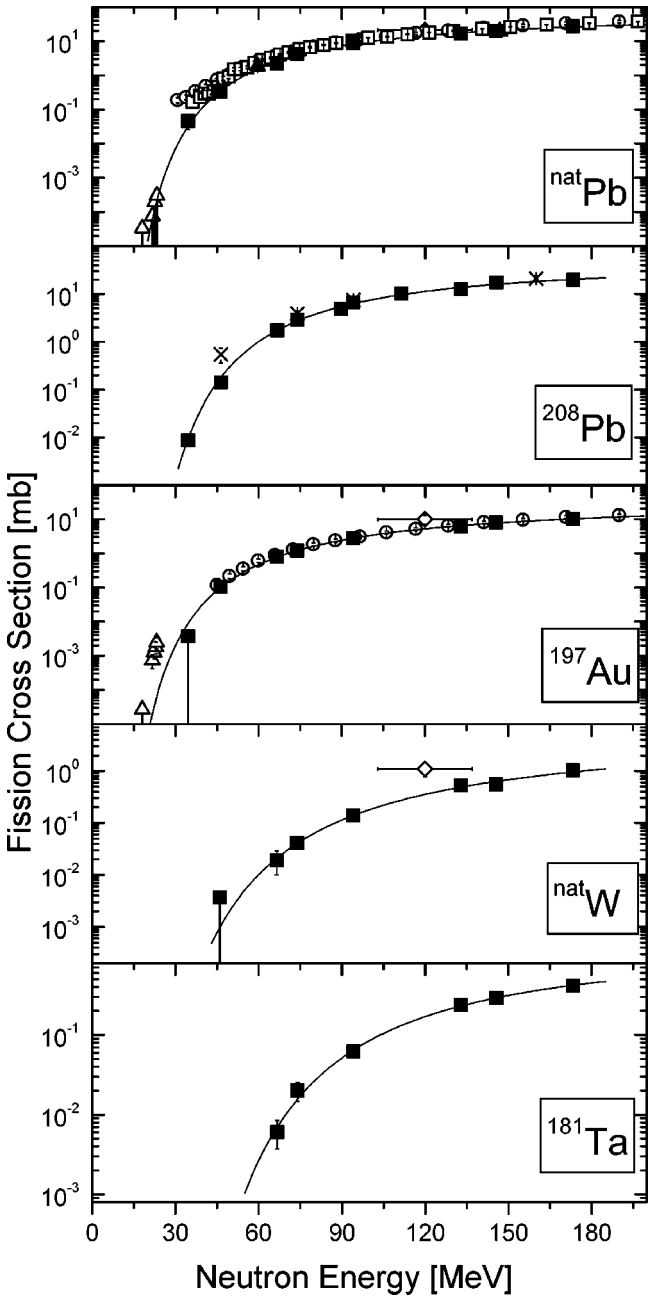

FIG. 11. Absolute neutron-induced fission cross sections of ^{nat}Pb, ^{208}Pb, ^{197}Au, ^{nat}W, and ^{181}Ta. The results of the present study are shown as filled squares. Crosses represent our earlier data for ^{208}Pb [21,22]. Filled triangles represent recent data of Nolte *et al.* for ^{nat}Pb [20]. Open squares, circles, and triangles represent data of Shcherbakov *et al.* [19], Staples *et al.* [17,18], and Vorotnikov *et al.* [14,15], respectively. Results of Reut *et al.* [12] and Dzhelepov *et al.* [13] are shown as diamonds, with horizontal error bars that represent the energy spread of the neutron beam. The lines represent parametrizations of the present work (see the text).

^{208}Pb(n,f) reaction has been studied by our group earlier [21,22], and those results, shown as crosses in Fig. 11, are in reasonable agreement with the present ones. The only exclusion is the datum at 45 MeV, which is believed to be erroneous in our early study, due to a poor signal-to-background ratio in that particular measurement. The present results are

TABLE VII. Parameters of the (n,f) cross-section parametrizations in Eq. (11).

Target nuclide	P_1 (mb)	P_2 (MeV)	P_3	χ^2/ν	Energy region of applicability (MeV)
^{209}Bi	109.2	131.5	1.32	1.33	30–180
^{nat}Pb	70.4	171.9	1.27	0.53	30–180
^{208}Pb	45.4	150.3	1.47	0.64	30–180
^{197}Au	35.0	207.2	1.18	0.09	45–180
^{nat}W	6.1	292.5	1.17	0.47	60–180
^{181}Ta	1.29	186.0	1.61	0.32	60–180

obtained with better counting statistics and more sophisticated data processing techniques.

Earlier measurements for ^{197}Au and ^{nat}Pb in the energy region 18–23 MeV were performed by Vorotnikov [15] and Vorotnikov and Larionov [14], respectively, using a *d-T* neutron source and solid-state nuclear track detectors. Their results for ^{nat}Pb are compatible with the present data, while the results for ^{197}Au seem to be too high.

A measurement for ^{nat}Pb and ^{197}Au was performed by Staples *et al.* [17,18] using a parallel-plate ionization chamber irradiated by neutrons from the LANSCE facility with a "white" spectrum. Only preliminary data are available. The data for ^{197}Au are in reasonable agreement with the present ones, while the data for ^{nat}Pb lie systematically higher. In the energy range below about 50 MeV, the data of Staples *et al.* for ^{nat}Pb are distinctly larger. The disagreement increases with decreasing incident energy and amounts to about one order of magnitude at 35 MeV. Furthermore, the ^{nat}Pb/^{209}Bi ratios deduced from the data of Staples *et al.* (see Fig. 10) show an unexpected energy dependence. As the neutron energy decreases to below 50 MeV, the smooth decrease of the ratio turns into a sharp rise, which is difficult to understand, having in mind that the fission barrier for lead isotopes is higher than that for bismuth [66]. This leads to the suggestion that some background contribution may not have been fully taken into account in the LANSCE measurements. A similar feature is seen in the dataset of Shcherbakov *et al.* for ^{nat}Pb [19] obtained at the "white" neutron source at the GNEIS facility in Gatchina. Their data are similar to the data of Staples *et al.* at neutron energies above about 45 MeV, although at lower energies they are somewhat closer to our results. The disagreement with our data amounts to a factor of about 3 at about 35 MeV.

Early measurements by Reut *et al.* [12] for ^{nat}Pb and ^{197}Au and by Dzhelepov *et al.* [13] for ^{nat}W were made using neutrons from the Cu(d,n) reaction with a broad spectrum, as indicated by the horizontal error bars in Fig. 11. The results agree qualitatively with the more recent and precise data.

The data presented in Fig. 11 allow some conclusions on common features of subactinide neutron fission cross sections. The cross section increases with neutron energy and with the atomic number of the target nucleus. The slope of the cross section versus energy is steepest in the near-barrier region (20–25 MeV), and becomes flatter with increasing energy. The slope at a specific incident energy is steeper for lighter nuclei. The properties summarized above (see also [24]) are similar to those of the (p,f) data (see, e.g., [9]).

VI. CONCLUSIONS

Experimental (n,f) cross sections for subactinide nuclei in the intermediate energy region have been measured. Most of the data are obtained for the first time. Progress in data processing has been achieved due to good control of the incident neutron spectrum and the detection efficiency corrections. In most cases, the results are compatible with scarcely available earlier data, but a large discrepancy is observed with respect to the recent data of Staples *et al.* [17,18] and Shcherbakov *et al.* [19] for the ^{209}Bi(n,f) and ^{nat}Pb(n,f) cross sections at energies below 50 MeV.

ACKNOWLEDGMENTS

The authors are thankful to the staff of The Svedberg Laboratory where the experimental part of the study was performed. The samples were partly provided and/or characterized by Dr. S.M. Soloviev, Dr. Yu.G. Pokrovskiy, and Dr. A.V. Gromov at V.G. Khlopin Radium Institute. The present work was supported in part by ISTC.

[1] H. Nifenecker, S. David, J. M. Loiseaux, and O. Meplan, Nucl. Instrum. Methods Phys. Res. A **463**, 428 (2001).
[2] A. J. Koning, J.-P. Delaroche, and O. Bersillon, Nucl. Instrum. Methods Phys. Res. A **414**, 49 (1998).
[3] Yu. N. Shubin, A. V. Ignatyuk, A. Yu. Konobeev, V. P. Lunev, and E. V. Kulikov, in *Proceedings of the 2nd Conference on ADTT, Kalmar, Sweden, 1996*, edited by H. Condé (Uppsala University, 1997), Vol. 2, p. 953.
[4] R. E. Prael, Trans. Am. Nucl. Soc. **73**, 349 (1995).
[5] A. V. Prokofiev, S. G. Mashnik, and A. J. Sierk, Nucl. Sci. Eng. **131**, 78 (1999).
[6] M. C. Duijvestijn, A. J. Koning, J. P. M. Beijers, A. Ferrari, M. Gastal, J. van Klinken, and R. W. Ostendorf, Phys. Rev. C **59**, 776 (1999).
[7] R. Michel and P. Nagel, NEA Report NSC/DOC(97)-1, January, 1997.
[8] W. U. Schröder and J. R. Huizenga, Nucl. Phys. **A502**, 473 (1989).
[9] A. V. Prokofiev, Nucl. Instrum. Methods Phys. Res. A **463**, 557 (2001).
[10] E. L. Kelly and C. Wiegand, Phys. Rev. **73**, 1135 (1948).
[11] V. I. Goldanskiy, V. S. Penkina, and E. Z. Tarumov, Sov. Phys. JETP **29**, 778 (1955) (in Russian).
[12] A. A. Reut, G. I. Selivanov, and V. V. Yuriev, Institute of

Nuclear Problems report, Moscow, 1950 (in Russian).
[13] V. P. Dzhelepov, B. M. Golovin, and Yu. M. Kazarinov, Institute of Nuclear Problems report, Moscow, 1950 (in Russian).
[14] P. E. Vorotnikov and L. S. Larionov, Sov. J. Nucl. Phys. **40**, 552 (1984).
[15] P. E. Vorotnikov, Sov. J. Nucl. Phys. **47**, 1147 (1988).
[16] H. Vonach, A. Pavlik, R. Nelson, and S. Wender (unpublished); R. E. Prael, Report LA-UR-94-1817, Los Alamos National Laboratory, 1994 (unpublished); H. Vonach (private communication).
[17] P. Staples, P. W. Lisowski, and N. W. Hill, presented in APS/AAPT Conference, Washington, D.C., 1995; Bull. Am. Phys. Soc. **40**, 962 (1995).
[18] P. Staples (private communication) (1996) with an update of the data from Ref. [17].
[19] O. Shcherbakov, A. Donets, A. Evdokimov, A. Fomichev, T. Fukahori, A. Hasegawa, A. Laptev, V. Maslov, G. Petrov, S. Soloviev, Y. Tuboltsev, and A. Vorobyev, J. Nucl. Sci. Technol. **2**, 230 (2002).
[20] R. Nolte, M. S. Allie, P. J. Binns, F. D. Brooks, A. Buffler, V. Dangendorf, K. Langen, J.-P. Meulders, W. D. Newhauser, F. Ross, and H. Schuhmacher, J. Nucl. Sci. Technol. **2**, 311 (2002).
[21] V. P. Eismont, A. V. Prokofiev, A. N. Smirnov, K. Elmgren, J. Blomgren, H. Condé, J. Nilsson, N. Olsson, T. Rönnqvist, and E. Tranéus, Phys. Rev. C **53**, 2911 (1996).
[22] V. P. Eismont, A. V. Prokofiev, A. N. Smirnov, J. Blomgren, H. Condé, K. Elmgren, J. Nilsson, N. Olsson, and E. Ramström, in *Proceedings of the 2nd International Conference on Accelerator Driven Transmutation Technologies and Applications, Kalmar, Sweden, 1996*, edited by H. Condé (Uppsala University, 1997), Vol. 2, p. 606.
[23] V. P. Eismont, A. V. Prokofiev, A. N. Smirnov, S. M. Soloviev, H. Condé, K. Elmgren, and N. Olsson, Proceedings of the 3rd International Conference on Accelerator Driven Transmutation Technologies and Applications, Praha (Pruhonice), Czech Republic, 1999 (available as CD-ROM, paper Mo-O-C8).
[24] V. P. Eismont (Project Manager), Measurements of Neutron-Induced Fission Cross Sections in Energy Region $15 < En < 160$ MeV for Basic and Applied Researches, Final Project Technical Report of ISTC 540-97, V.G.Khlopin Radium Institute, St.-Petersburg, 1999.
[25] V. P. Eismont, I. V. Ryzhov, A. N. Smirnov, G. A. Tutin, H. Condé, N. Olsson, and A. V. Prokofiev, Proceedings of the 6th OECD/NEA Information Exchange Meeting on Actinide and Fission Product Partitioning and Transmutation, Madrid, 2000 (available as CD-ROM, paper 36).
[26] A. Prokofiev, Ph.D. thesis, Uppsala University (2001).
[27] V. P. Eismont, A. V. Kireev, I. V. Ryzhov, G. A. Tutin, H. Condé, K. Elmgren, and S. Hultqvist, in *Proceedings of the 2nd International Conference on Accelerator Driven Transmutation Technologies and Applications, Kalmar, Sweden, 1996*, edited by H. Condé (Uppsala University, 1997), Vol. 2, p. 618.
[28] V. P. Eismont, A. V. Kireev, I. V. Ryzhov, S. M. Soloviev, G. A. Tutin, H. Condé, K. Elmgren, N. Olsson, and P.-U. Renberg, Proceedings of the 3rd International Conference on Accelerator Driven Transmutation Technologies and Applications, Praha, Czech Republic, 1999 (available as CD-ROM, paper Mo-O-C7).
[29] I. V. Ryzhov, G. A. Tutin, V. P. Eismont, A. G. Mitryukhin, V. S. Oplavin, S. M. Soloviev, H. Condé, N. Olsson, and P.-U. Renberg, J. Nucl. Sci. Technol. **2**, 1410 (2002).
[30] R. K. Jain, A. V. Prokofiev, A. N. Smirnov, and L. Tommasino, Radiat. Meas. **34**, 129 (2001).
[31] A. V. Prokofiev, S. G. Mashnik, M. B. Chadwick, N. Olsson, and L. S. Waters, J. Nucl. Sci. Technol. **2**, 112 (2002).
[32] V. P. Eismont (Project Manager), Measurements and Comparison of Proton- and Neutron-Induced Fission Cross Sections of Lead and Neighboring Nuclei in the 20-200 MeV Energy Region, Final Project Technical Report of ISTC 1309-99, V.G. Khlopin Radium Institute, St.-Petersburg, 2002.
[33] V. P. Eismont, A G. Mitryukhin, V. S. Oplavin, I. V. Ryzhov, A. N. Smirnov, S. M. Solovjev, G. A. Tutin, H. Conde, N. Olsson, O. Jonson, and P.-U. Renberg, TSL Progress Report 2000–2001, edited by A. Ingemarsson (Uppsala University, 2002), p. 42; A. N. Smirnov, N. P. Filatov, A. V. Prokofiev, and P.-U. Renberg (unpublished).
[34] A. D. Carlson, S. Chiba, F.-J. Hambsch, N. Olsson, and A. N. Smirnov, IAEA Report INDC(NDS)-368, Vienna, 1997; Proceedings of the International Conference on Nuclear Data for Science and Technology, Trieste, Italy, 1997, Part II, p. 1223.
[35] H. Condé, S. Hultqvist, N. Olsson, T. Rönnqvist, R. Zorro, J. Blomgren, G. Tibell, A. Hakånsson, O. Jonsson, A. Lindholm, L. Nilsson, P.-U. Renberg, A. Brockstedt, P. Ekström, M. Österlund, F. P. Brady, and Z. Szeflinski, Nucl. Instrum. Methods Phys. Res. A **292**, 121 (1990).
[36] J. Klug, J. Blomgren, A. Atac, B. Bergenwall, S. Dangtip, K. Elmgren, C. Johansson, N. Olsson, A. V. Prokofiev, J. Rahm, O. Jonsson, L. Nilsson, P.-U. Renberg, P. Nadel-Turonski, A. Ringbom, A. Oberstedt, F. Tovesson, C. Le Brun, J. F. Lecolley, F. R. Lecolley, M. Louvel, N. Marie, C. Schweitzer, C. Varignon, Ph. Eudes, F. Haddad, M. Kerveno, T. Kirchner, C. Lebrun, L. Stuttge, I. Slypen, A. N. Smirnov, R. Michel, S. Neumann, and U. Herpers, Nucl. Instrum. Methods Phys. Res. A **489**, 282 (2002).
[37] J. F. Ziegler, J. P. Biersack, and U. Littmark, *The Stopping and Range of Ions in Solids* (Pergamon Press, New York, 1985).
[38] S. Neumann, Ph.D. thesis, University of Hannover (1999); R. Michel, W. Glasser, S. Neumann, A. N. Smirnov, A. V. Prokofiev, P. Malmborg, and O. Jonsson, The Svedberg Laboratory Progress Report 1998-1999, Uppsala, 2000, p. 20 (unpublished).
[39] T. Rönnqvist (private communication).
[40] R. C. Byrd and W. C. Sailor, Nucl. Instrum. Methods Phys. Res. A **274**, 494 (1989).
[41] S. Stamer, W. Scobel, and R. C. Byrd, Proceedings of a Specialists' Meeting on Neutron Cross-Section Standards for the Energy Region above 20 MeV, Uppsala, Sweden, 1991, NEANDC-305/U, p. 154.
[42] N. Nakao, Y. Uwamino, T. Nakamura, T. Shibata, N. Nakanishi, M. Takada, E. Kim, and T. Kurosawa, Nucl. Instrum. Methods Phys. Res. A **420**, 218 (1999).
[43] M. Baba, Y. Nauchi, T. Iwasaki, T. Kiyosumi, M. Yoshioka, S. Matsuyama, N. Hirakawa, T. Nakamura, Su. Tanaka, S. Meigo, H. Nakashima, Sh. Tanaka, and N. Nakao, Nucl. Instrum. Methods Phys. Res. A **428**, 454 (1999).
[44] H. Schuhmacher, H. J. Brede, V. Dangendorf, M. Kuhfuss, J. P. Meulders, W. D. Newhauser, and R. Nolte, Nucl. Instrum. Methods Phys. Res. A **421**, 284 (1999).
[45] R. Nolte, M. S. Allie, P. J. Binns, F. Brooks, A. Buffler, V.

Dangendorf, J. P. Meulders, F. Roos, H. Schuhmacher, and B. Wiegel, Nucl. Instrum. Methods Phys. Res. A **476**, 369 (2002).
[46] G. G. Ohlsen, Nucl. Instrum. Methods **37**, 240 (1965).
[47] S. D. Schery, L. E. Young, R. R. Doering, S. M. Austin, and R. K. Bhowmik, Nucl. Instrum. Methods **147**, 399 (1977).
[48] H. Orihara, S. Nishihara, K. Furukawa, M. Kabasawa, T. Kawamura, Y. Takahashi, T. Nakagawa, and K. Maeda, Nucl. Instrum. Methods Phys. Res. A **257**, 189 (1987).
[49] C. J. Batty, B. E. Bonner, E. Friedman, C. Tschalar, L. E. Williams, A. S. Clough, and J. B. Hunt, Nucl. Phys. **A120**, 297 (1968).
[50] J. W. Watson, B. D. Anderson, A. R. Baldwin, C. Lebo, B. Flanders, W. Pairsuwan, R. Madey, and C. C. Foster, Nucl. Instrum. Methods Phys. Res. **215**, 413 (1983).
[51] X. Yang, L. Wang, J. Rapaport, C. D. Goodman, C. C. Foster, Y. Wang, E. Sugarbaker, D. Marchlenski, S. de Lucia, B. Luther, L. Rybarcyk, T. N. Taddeucci, and B. K. Park, Phys. Rev. C **52**, 2535 (1995).
[52] S. G. Mashnik, M. B. Chadwick, P. G. Young, R. E. MacFarlane, and L. S. Waters, LANL Report LA-UR-00-1067, Los Alamos (2000) (unpublished); presented at 2000 ANS/ENS International Meeting, Nuclear Applications of Accelerator Technology (AccApp00), November 12-16, Washington, D.C.; http://xxx.lanl.gov/e-print/nucl-th/0011066.
[53] M. B. Chadwick, P. G. Young, S. Chiba, S. C. Frankle, G. M. Hale, H. G. Hughes, A. J. Koning, R. C. Little, R. E. MacFarlane, R. E. Prael, and L. S. Waters, Nucl. Sci. Eng. **131**, 293 (1999).
[54] C. Kalbach, Phys. Rev. C **37**, 2350 (1988).
[55] V. P. Eismont, A. V. Prokofiev, and A. N. Smirnov, Radiat. Meas. **25**, 151 (1995).
[56] V. A. Nikolaev, Radiat. Meas. **25**, 337 (1995).
[57] V. P. Eismont and A. N. Smirnov, Prib. Tekh. Eksp. **6**, 5 (1983) (in Russian).
[58] C. M. Zoller, Ph.D. thesis, University of Darmstadt (1995) (in German).
[59] Yu. P. Gangrskiy, B. Dalhsuren, and B. N. Markov, *Nuclear Fission Fragments* (Energoatomizdat, Moscow, 1986) (in Russian).
[60] M. C. Duijvestijn, A. J. Koning, and F.-J. Hambsch, Phys. Rev. C **64**, 014607 (2001).
[61] V. E. Viola, K. Kwiatkowski, and M. Walker, Phys. Rev. C **31**, 1550 (1985).
[62] L. C. Northcliffe and R. F. Schilling, At. Data Nucl. Data Tables **A7**, 233 (1970).
[63] O. Jonsson, P.-U. Renberg, A. Prokofiev, and A. Smirnov, TSL Progress Report 1998-1999, edited by A. Ingemarsson, Uppsala University (2000), p. 43 (unpublished).
[64] K. Johansson, P. Dyreklev, B. Granbom, N. Olsson, J. Blomgren, and P.-U. Renberg, IEEE Trans. Nucl. Sci. **45**, 2519 (1998).
[65] K.-H. Schmidt, C.-C. Sahm, K. Pielenz, and H.-G. Clerc, Z. Phys. A **316**, 29 (1984).
[66] A. V. Ignatyuk, G. N. Smirenkin, M. G. Itkis, S. I. Mulgin, and V. N. Okolovich, Sov. J. Part. Nucl. **16**, 307 (1985).